

Determining surface structure and stability of ϵ -Fe₂C, χ -Fe₅C₂, θ -Fe₃C and Fe₄C phases under carburization environment from combined DFT and atomistic thermodynamic studies

Shu Zhao, Xing-Wu Liu, Chun-Fang Huo, Yong-Wang Li, Jianguo Wang & Haijun Jiao

To cite this article: Shu Zhao, Xing-Wu Liu, Chun-Fang Huo, Yong-Wang Li, Jianguo Wang & Haijun Jiao (2015) Determining surface structure and stability of ϵ -Fe₂C, χ -Fe₅C₂, θ -Fe₃C and Fe₄C phases under carburization environment from combined DFT and atomistic thermodynamic studies, *Catalysis, Structure & Reactivity*, 1:1, 44-60, DOI: [10.1179/2055075814Y.0000000007](https://doi.org/10.1179/2055075814Y.0000000007)

To link to this article: <https://doi.org/10.1179/2055075814Y.0000000007>



© 2015 The Author(s). Published by Taylor & Francis



[View supplementary material](#)



Published online: 03 Dec 2014.



[Submit your article to this journal](#)



Article views: 2861



[View related articles](#)



[View Crossmark data](#)



Citing articles: 20 [View citing articles](#)

Determining surface structure and stability of ϵ -Fe₂C, χ -Fe₅C₂, θ -Fe₃C and Fe₄C phases under carburization environment from combined DFT and atomistic thermodynamic studies

Shu Zhao^{1,2,3}, Xing-Wu Liu^{1,2,3}, Chun-Fang Huo^{1,2}, Yong-Wang Li^{1,2}, Jianguo Wang¹ and Haijun Jiao^{*1,4}

¹State Key Laboratory of Coal Conversion, Institute of Coal Chemistry, Chinese Academy of Sciences, Taiyuan 030001, China

²National Energy Center for Coal to Liquids, Synfuels China Co., Ltd, Huairou District, Beijing 101400, China

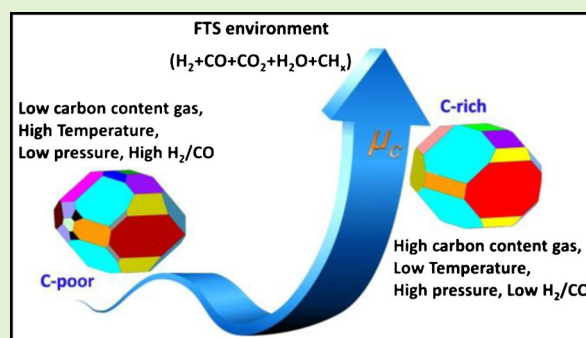
³University of Chinese Academy of Sciences, No. 19A Yuquan Road, Beijing 100049, China

⁴Leibniz-Institut für Katalyse e.V. an der Universität Rostock, Albert-Einstein Strasse 29a, 18059 Rostock, Germany

Abstract The chemical–physical environment around iron based FTS catalysts under working conditions is used to estimate the influences of carbon containing gases on the surface structures and stability of ϵ -Fe₂C, χ -Fe₅C₂, θ -Fe₃C and Fe₄C from combined density functional theory and atomistic–thermodynamic studies. Higher carbon content gas has higher carburization ability; while higher temperature and lower pressure as well as higher H₂/CO ratio can suppress carburization ability. Under wide ranging gas environment, ϵ -Fe₂C, χ -Fe₅C₂ and θ -Fe₃C have different morphologies, and the most stable non-stoichiometric termination changes from carbon-poor to carbon-rich (varying surface Fe/C ratio) upon the increase in $\Delta\mu_C$. The most stable surfaces of these carbides have similar surface bonding pattern, and their surface properties are related to some common phenomena of iron based catalysts. For these facets, χ -Fe₅C₂-(100)-2.25 is most favored for CO adsorption and CH₄ formation, followed by θ -Fe₃C-(010)-2.33, ϵ -Fe₂C-($\bar{1}\bar{2}1$)-2.00 and Fe₄C-(100)-3.00, in line with surface work function and the charge of the surface carbon atoms.

Keywords Iron carbides, Carburization, Morphology, Fischer–Tropsch synthesis, DFT

Cite this article S. Zhao, X. W. Liu, C. F. Huo, Y. W. Li, J. Wang and H. Jiao: *Catal. Struct. React.*, 2015, 1, 44-59



Introduction

Fischer–Tropsch synthesis (FTS) is an important technology in converting synthesis gas generated from coal, natural gas and biomass into oil and value added chemicals.¹ Almost a hundred years after its discovery, FTS has been attracting increasing interest worldwide due to the increasing oil prices. Despite of the large scale industrial applications and extensive studies on this important technology in the past decades, the detailed FTS mechanisms are still not fully understood and many explanations to the experimental

observations are premature and lack of scientific rationalization. One of these uncertainties is the surface structures, the corresponding active sites and their roles under FTS conditions.

Suitable FTS catalysts for industrial applications are iron or cobalt based, and iron based catalysts may become more dominant along with the expanding of FTS capacity due to the higher availability and lower cost of iron compared to cobalt. Freshly prepared iron based FTS catalysts are generally iron oxides [mainly hematite (α -Fe₂O₃) and also small amount of maghemite (γ -Fe₂O₃) or even ferrihydrate] and they have to be reduced before becoming FTS active. During the reduction, α -Fe₂O₃ is firstly reduced to magnetite

*Corresponding author, email haijun.jiao@catalysis.de

(Fe₃O₄) by using H₂, synthesis gas or CO and then partially transferred to metallic iron and iron carbides in varying proportions depending on the operating conditions.^{2,3} Such multiple phases with very fine crystalline dimensions (several to tens of nanometers) make the characterization and identification of the active phases very difficult, and often such phases will change once the environment around changes as found in most *ex situ* analyses. This leads to the misunderstanding and misinterpretation of the experimentally observed phenomena from real FTS reaction tests.⁴

In Fe based FTS, ε -Fe₂C, χ -Fe₅C₂ and θ -Fe₃C phases have been detected experimentally.^{3,5} Both ε -Fe₂C and χ -Fe₅C₂ phases have a hexagonally close packed structure^{6,7} but differ in interstitial carbon sites. In ε -Fe₂C, the carbon atom is in the iron octahedral center, while in θ -Fe₃C and χ -Fe₅C₂, the carbon atom is in the iron trigonal prismatic center. Hexagonal carbide (ε -Fe₂C) has been identified as the carburization product of H₂ reduced iron and CO at low temperature,⁸ and is the sole component up to 520 K and stable up to 600 K.^{8,9} Not formed during FTS at low temperature (<575 K),¹⁰ θ -Fe₃C is only found after carburization above 720 K.^{11,12} Under both CO and synthesis gas, ε -Fe₂C is considered as χ -Fe₅C₂ precursor, which is subsequently transformed into θ -Fe₃C at high temperature.^{8,13} Königer *et al.*⁶ observed that ε -Fe₂C can be converted to χ -Fe₅C₂ after annealing at 423 K, and the χ -Fe₅C₂ phase starts to transform to θ -Fe₃C at 573 K, which is the dominant phase after annealing at 723 K.⁶ The exact transformation temperature for the formation of the specific carbide phases depends on many factors, such as crystallite size, morphology, surface texture and promoters or inhibitors as well as the other environment conditions (pressure and gas composition). By using *ab initio* atomistic thermodynamics to investigate the stability of bulk carbide phases, de Smit *et al.*,³ found that the stable carbide phases depend highly on carbon chemical potential (μ_C) imposed by gas phase surroundings and emphasized the importance of the controlling chemical–physical environment around the catalyst for forming an efficient FTS system.

Despite the fact that pretreatments can affect the catalytic performance of iron based catalysts, the corresponding studies of the surface properties along with the change of the gas environment (or chemical potential) are rare and most have focused on the defined stoichiometric terminations and the non-stoichiometric terminations of carbides have not been considered.^{14,15} The stability and structure as well as electronic and magnetic properties of ε -Fe₂C^{16–18} and θ -Fe₃C^{14,19–22} have been investigated intensively. In addition, the adsorption and activation of CO and H₂ as well as C_xH_y formation on the (100), (001) and (010) surfaces of Fe₃C have been computed.^{23–26} Although not directly detected under FTS conditions, Fe₄C can be formed by incorporating carbon atoms into the face centered cubic γ -iron lattices²⁷ and we included Fe₄C in our study for comparison. The properties of the (100), (110), (111) surfaces of Fe₄C²⁸ and the CO adsorption properties on these surfaces also have been investigated in our previous work.²⁹ Recently we found that pretreating conditions, such as temperature, pressure and H₂/CO ratios of an idealized and closed equilibrium system, have significant impact on the relative stability of the

χ -Fe₅C₂ facets in different Fe/C ratios.³⁰ However, the effects of non-idealized and wide varying operating environments on surface composition and stability of other iron carbides (ε -Fe₂C, θ -Fe₃C and Fe₄C) have not ever been considered. In fact, the real FTS chemical–physical environment may result in wide varying non-equilibrium nature for the catalytic system and the change trends of the catalyst phases will be driven by carbon chemical potential (μ_C) under conditions with complicated mechanisms. Although the gas environment may result in non-equilibrium, the catalysts can be considered to reach the steady state for a continuous flow of reactants and products at defined conditions. For a fundamental understanding into the FTS mechanisms, systematic studies of the relationship between catalyst surface structures and the thermodynamic parameters for pushing surface structure evolution on the basis of the FTS environment are highly desired.

In this work, the surface structure and stability of the ε -Fe₂C, θ -Fe₃C and Fe₄C as well as χ -Fe₅C₂ phases have been investigated on the basis of density functional theory (DFT) calculations and atomistic thermodynamics by considering the influence of temperature, pressure and H₂/CO ratio under simplified and wide varying non-equilibrium environment. The CO activation and the reactivity analysis on the obtained stable surfaces are also conducted aiming at approaching the overall landscape of Fe based FTS catalysts under real operating conditions.

Methodology

Structure calculation

The catalyst structures were calculated at the level of DFT with Vienna *ab initio* simulation package.^{31,32} Electron exchange and correlation energy was treated within the generalized gradient approximation and the Perdew–Burke–Ernzerhof scheme (PBE).³³ Electron ion interaction was described by the projector augmented wave method.^{34,35} Spin polarization was included in all calculations on the ferromagnetic iron carbide systems (ε -Fe₂C, θ -Fe₃C and Fe₄C) and this is essential for an accurate description of the magnetic properties. Iterative solutions of the Kohn–Sham equations were done using a plane wave basis with energy cutoff of 400 eV, and the samplings of the Brillouin zone were generated from the Monkhorst–Pack scheme. A second order Methfessel–Paxton³⁶ electron smearing with $\sigma=0.2$ eV was used to ensure accurate energies with errors due to smearing of less than 1 meV per unit cell. The convergence criteria for the force and electronic self-consistent iteration were set to 0.03 eV Å⁻¹ and 10⁻⁴ eV, respectively.

Catalyst models

The bulk structures and the corresponding Monkhorst–Pack grid of k points of the ε -Fe₂C, θ -Fe₃C and Fe₄C phases are listed in Table 1. The optimized lattice parameters agree well with those of the experiments and other calculations.^{23,28,37–41} In calculating the ε -Fe₂C bulk structure, a 2 × 2 × 1 supercell was used, and the detailed information is given in the Appendix. For all surface calculations, symmetrical slab surface models were chosen. Each surface was represented by a slab in 10–15 Å thickness, enough to avoid significant influence on the surface energies from our benchmarks.³⁰ A

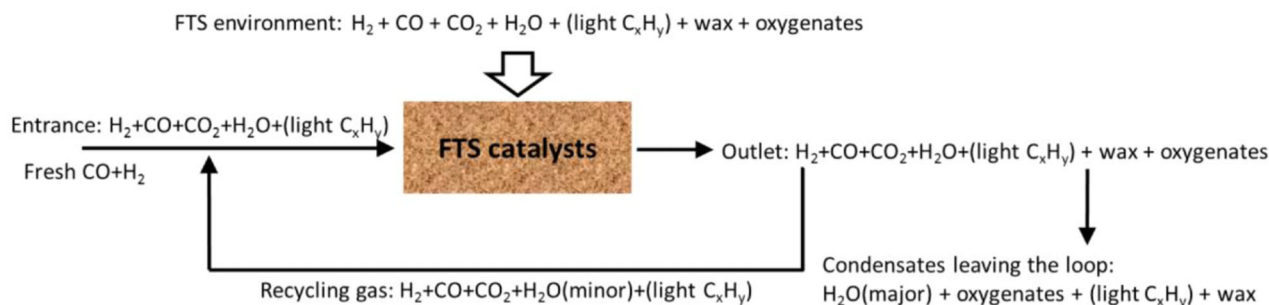


Figure 1 Overall scheme of complicated chemical environment of FTS reactions

vacuum layer of 15 Å was set to exclude the interactions among the periodic slabs, and all atoms were fully relaxed during the calculations. The Monkhorst–Pack grid of k points for each of the corresponding slab models is included in the Supplementary Material (Table S1).

Atomistic thermodynamics

The surface stability influenced by temperature, pressure and gas composition was investigated by using *ab initio* atomistic thermodynamics.^{42,43} Since this is the same procedure used in our previous study on the surface composition and morphology of the χ -Fe₅C₂ phase,³⁰ detailed information can be found either in the Supplementary Material or in our previous work. Using the total energy of an isolated carbon atom (E_C) as reference for the variable μ_C , $\Delta\mu_C = \mu_C - E_C$, the minimum $\Delta\mu_C$ for the ε -Fe₂C, χ -Fe₅C₂,³⁰ θ -Fe₃C and Fe₄C phases is -7.83 , -7.80 , -7.80 and -8.01 eV, respectively. The total energies of gas phase molecules and carbon atom were calculated using a single k point (gamma point), where the periodic molecules were separated with 15 Å vacuum distances. These critical $\Delta\mu_C$ values indicate the lowest μ_C for the formation of stable carbides. Since the vibrational contribution to the Gibbs free energy of the χ -Fe₅C₂ slab is negligible³⁰ and this is also true for most solid matter, we used only the total energy (E_{slab}) as the predominant term obtained directly from DFT calculations.

CO adsorption

For systematic comparison of the surface properties, we computed CO adsorption on the most stable facets of these carbides. The adsorption energy per CO molecule (E_{ads}) is

defined as $E_{\text{ads}} = [E_{\text{CO/slab}} - (nE_{\text{CO}} + E_{\text{slab}})]/n$; where $E_{\text{CO/slab}}$, E_{CO} and E_{slab} are the total energies of the slab with adsorbed CO on the surface, an isolated CO molecule and the slab of the clean surface, respectively, and n is the number of adsorbed CO molecules. The coverage (θ) is defined as the number of CO molecules over the number of the exposed layer iron atoms. The surface C atoms (C_s) of iron carbides can be considered as adatoms on the defective surfaces, and the binding energy of C_s can be obtained as $E_{\text{ads}}(C_s) = E_{\text{slab}} - E_{\text{slab/defect}} - E_C$, where E_{slab} , $E_{\text{slab/defect}}$ and E_C are the total energies of the slab, the defective slab and an isolated carbon atom, respectively. Since PBE functional can give reasonable optimized geometries but overestimates the adsorption energies,⁴⁴ we used PBE for structure optimization and RPBE single point energy for estimating the adsorption energy. The Bader charges are used for discussing the effects of charge transfer.^{45–47}

Results and discussion

Carbon chemical potential (μ_C) models for real FTS environment

The chemical–physical environment of real FTS catalysts should be properly defined in terms of the operating conditions. Our focus is on the trend of the phase transition of iron carbides in FTS reaction, for which the iron based catalysts have been treated as iron carbides obtained from reduction steps.^{3,8,11} For this purpose, the driving force of the phase transition of iron carbides is μ_C , which can be defined using *ab initio* atomistic thermodynamics. Due to the complicated phenomena of the carburization processes,^{3,48}

Table 1 Bulk properties of iron carbides (experimental values in parentheses) and used Monkhorst–Pack grid of k points

Crystal	Cell parameters	μ_B (Fe)
ε -Fe ₂ C Hexagonal <i>P63/mmc</i> (5 × 5 × 6)	$a = 5.472$ Å (2 × 2.794 Å)* $b = 5.639$ Å (2 × 2.794 Å)* $c = 4.280$ Å (4.360 Å)* $\beta = 121.0^\circ$ (120.0°)*	1.66 (1.70–1.72)§
θ -Fe ₃ C Orthorhombic <i>Pnma</i> (7 × 5 × 9)	$a = 5.025$ Å (5.080 Å)†	1.91 (1.72–1.79)§
Fe ₄ C Cubic <i>Pm$\bar{3}m$</i> (7 × 7 × 7)	$b = 6.726$ Å (6.730 Å)† $c = 4.471$ Å (4.510 Å)† $\beta = 90.0^\circ$ (90.0°)† $a = 3.761$ Å (3.750 Å)‡	Fe(I): 3.04, Fe(II): 1.75

*Ref. 37.

†Ref. 38.

‡Ref. 39.

§Ref. 41.

many species in FTS system can either increase or decrease μ_C imposed over the iron based catalyst surfaces, as discussed in previous studies.⁴⁹⁻⁵⁵ A comprehensive modeling of the chemical-physical environment of real FTS catalysts should consider most of the key factors, which will have normally non-linear type of contribution to the phase transition phenomena to be investigated. With this in mind, it is necessary to recall the schemes of a real FTS process as Fig. 1.

As given in Fig. 1, the chemical species involved in real FTS system include hydrogen, carbon monoxide, carbon dioxide, water and hydrocarbons within a wide carbon number distribution as well as small portions of oxygenates (mainly alcohols). The composition of these chemical species can easily be determined from industrial operation measurements and/or detailed material balance calculations for a real FTS system. This defines the rather accurate boundaries of the chemical-physical environment around working FTS catalysts, and the catalyst evolution trend may be predicted by using *ab initio* atomistic thermodynamics. For this goal, the key issue is to systematically develop the model to describe μ_C over the surfaces imposed by environment. However, this model is not very straight forward because of the wide varying and non-equilibrium nature of real FTS systems, namely the theoretical trends of the change in catalyst structures will largely depend on the kinetic factors of all the events related to the chemical species in the catalyst phases, and these events cover both carburization and decarburization reactions. Table 2 lists an overall summary of the events relating to the possible reactions between the catalyst phases (C_s) and the chemical species.

It should be noted that the reactions in Table 2 may occur thermodynamically under typical FTS conditions and affect μ_C . In fact the exact behaviors of μ_C will be also highly related to the rates of these reactions under FTS conditions. However, one can always study the thermodynamic trends by using energetics on the basis of the data from *ab initio* atomistic thermodynamics.

Obviously, CO is the most potential carburization agent in FTS and can easily deposit carbon atoms on the iron surface from the Boudouard reaction (2CO → C + CO₂, reaction (2)). Gas phase molecular hydrogen and the adsorbed hydrogen which plays important roles in the transition of catalyst phases are in equilibrium.⁵⁶ Oxygen removal from the surface is rate limiting for carbide formation in pure CO, but this step becomes rapid in the presence of hydrogen, therefore addition of H₂ to CO can accelerate carbon deposition (CO + H₂ → C_s + H₂O, reaction (3)).^{57,58} However, the most important role of H₂ is the hydrogenation of surface carbon atoms (C_s + H₂ → -CH₂-, reaction (1)) resulting in hydrocarbons as the primary products of FTS.^{50,56} On the other hand, the light C_xH_y can also be transferred into surface carbons (-CH₂- → C_s + H₂, reaction (7),^{57,59} and 2(-CH₂-) + CO₂ → 3C_s + 2H₂O, reaction (8)). In addition, CO₂ can also consume hydrogen (CO₂ + 2H₂ → C_s + 2H₂O, reaction (5)), and the reaction extent is limited by water content and temperature.^{50,58} Otherwise, CO₂ and H₂O as byproducts can act as decarburizing agents (C_s + CO₂ → 2CO, reaction (4); and C_s + H₂O → CO + H₂, reaction (6)). The presence of CO₂ even in small quantities requires high CO concentration to

balance this decarburizing reaction at elevated temperature.⁴⁸

It is suggested that reaction (3) has the fastest kinetics on the basis of the high metal dusting rates in CO/H₂ environment,^{48,55,57,59} while reaction (2) is also rapid and the rate of carbon deposition decreases with the increasing CO₂ content.⁵³ Olsson and Turkdogan⁵³ showed that in CO-H₂ mixtures reaction (2) is most important for H₂ content less than 50%, while the contribution of reaction (3) to the total rate is dominant for more than 50% H₂. In their study, H₂O has great influence on the rate of carbon deposition. When H₂O is added into CO-H₂ mixture, the rate of carbon deposition decreases with the increasing water vapor content, and this is due to reaction (6) (the reverse of reaction (3)). On the other hand, under CO condition, the rate of reaction (2) increases with the increasing H₂O content.⁵³ Koeken *et al.*,⁶⁰ found that increasing the total pressure can increase carbon deposition rate for a H₂/CO ratio of 1 : 1, but when H₂/CO ratio is higher than 4 : 1, higher total pressure can suppress the carbon deposition, and increasing H₂/CO ratio can also decrease the rate of carbon deposition. Ando and Kimura⁶¹ also found that the amount of deposited carbon on iron apparently increases by adding small amount of H₂ to pure CO, while an excessive H₂ retards carbon deposition. These results imply that the carbon deposition rate is sensitive to the operating conditions (temperature, pressure and gas composition).

Apart from reactions (2) and (3), we also considered the carbon transfer from light hydrocarbons (C_xH_y) in reaction (7) (C_xH_y → xC_(Fe) + y/2H₂) to estimate their carburization ability. In this case, μ_C [$\mu_C = 1/x(\mu_{C_xH_y} - y/2\mu_{H_2})$] is determined by decomposition of light hydrocarbon. The influences of temperature, pressure and H₂/C_xH_y ratio on $\Delta\mu_C$ are given in Fig. 2. As temperature increases from 450 to 650 K at 30 atm with a 15% molar percentage of C_xH_y (Fig. 2a), $\Delta\mu_C$ changes hardly under C₂H₄ and C₂H₆ as gas reservoirs, while slightly decreases under C₂H₂ and increases under

Table 2 List of possible reactions between catalyst phases (C_s) and FTS species

Species	Events	Effect§
H ₂	C _s + H ₂ → -CH ₂ -	(1)* -
CO	2CO → C _s + CO ₂	(2)† +
	CO + H ₂ → C _s + H ₂ O	(3)‡ +
CO ₂	C _s + CO ₂ → 2CO	(4)† -
	CO ₂ + 2H ₂ → C _s + 2H ₂ O	(5) +
H ₂ O	C _s + H ₂ O → CO + H ₂	(6)‡ -
-CH ₂ -	-CH ₂ - → C _s + H ₂	(7) +
	2(-CH ₂ -) + CO ₂ → 3C _s + 2H ₂ O	(8) +

*Molecular hydrogen may undergo rapid decomposition (H₂ → 2H_s) on catalyst surfaces and surface hydrogen atoms may hydrogenate surface carbon atoms (FTS key steps).

†Under CO-CO₂ mixture, the carburizing mechanism consists of two elementary reactions: CO → C_s + O_s and CO + O_s → CO₂, the later one was found to be rate limiting.

‡Hydrogen has been shown to be an accelerator of CO decomposition over iron based catalysts, while H₂O has been found to both accelerate and retard CO decomposition.⁷⁵ The rates of reactions (2) and (3) depend on the rates of the reactions of CO and H₂ with an oxygen atom to produce CO₂ and H₂O, respectively.⁷⁶

§Positive effect (+) for carburization, and negative effect (-) for decarburization.

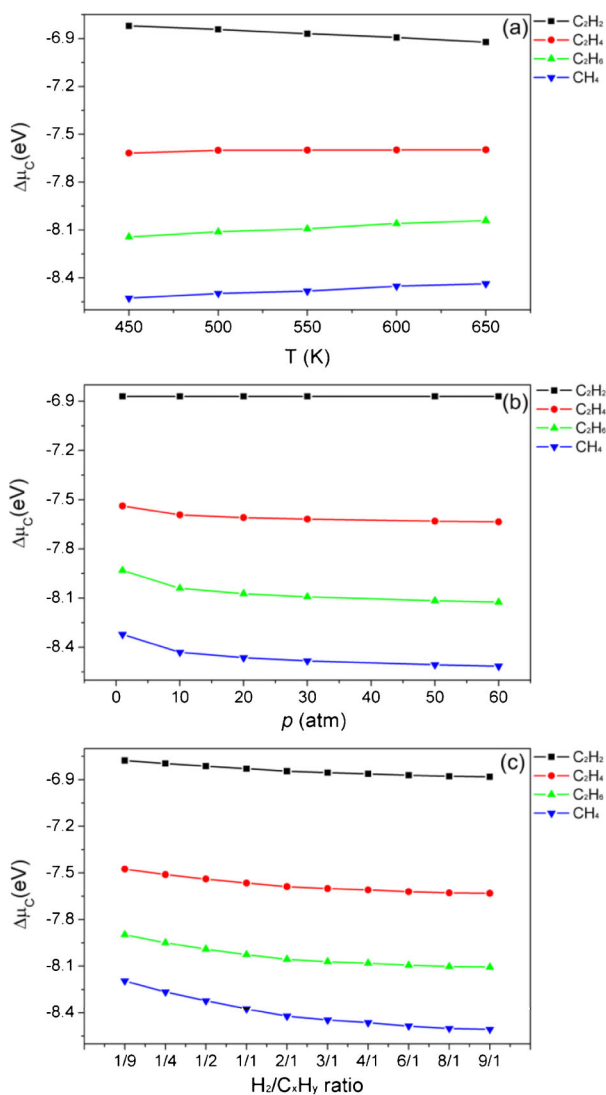


Figure 2 Relationship of carbon chemical potential ($\Delta\mu_C$) to **a** temperature (450–650 K) at 30 atm and $C_xH_y=15\%$; **b** total pressure (1–60 atm) at 550 K and $C_xH_y=15\%$; **c** H_2/C_xH_y ratio (1/9 to 9/1) at 550 K and 30 atm under hydrocarbons

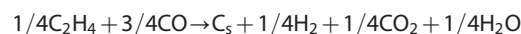
CH_4 . As the pressure rises from 1 to 60 atm at 550 K with a 15% molar percentage of C_xH_y (Fig. 2b), $\Delta\mu_C$ slightly decreases under C_2H_4 , C_2H_6 and CH_4 , while does not change under C_2H_2 . As expected, increasing the H_2/C_xH_y ratio from 1/9 to 9/1 at 550 K and 30 atm lowers $\Delta\mu_C$ in some extent (Fig. 2c).

Figure 2 shows that the carburization ability of light hydrocarbons decreases with the decrease in carbon content from acetylene to saturated hydrocarbons, i.e. $C_2H_2 > C_2H_4 > C_2H_6 > CH_4$. It is noted that $\Delta\mu_C$ under saturated hydrocarbons (C_2H_6 and CH_4) becomes lower than the critical values for stable iron carbide phases, i.e. -7.83 eV for ϵ -Fe₂C, -7.80 eV for χ -Fe₅C₂³⁰ and θ -Fe₃C as well as -8.01 eV for Fe₄C, and consequently the carbide phases will transform to metallic iron phase. Therefore, we used ethylene as light hydrocarbon model for our discussion and comparison.

The μ_C to real FTS catalysts can be estimated under different conditions relating to the possible modes, e.g. hydrogen rich modes for starting-up and shutdown of the process, the normal modes typically for oil production, and

CO rich mode due to some unexpected reasons in the whole process. In this work, we try to understand the tendency of the change of the iron carbide phases in the above major situations. As discussed above, in CO/H₂ mixture, only reactions (2), (3) and (7) can contribute to carbon deposition at different levels (Table 2) and their reversible reactions can give overall description of the major physical and chemical relations to carbon deposition on real FTS catalysts. By considering only reaction (3) ($CO + H_2 \rightarrow C + H_2O$), the $\Delta\mu_C$ is much higher than the minimum of carbides (-7.80 eV). It is also true by raising the H₂/CO ratio from 1/1 to 100/1, the $\Delta\mu_C$ (from -6.76 to -6.91 eV) is still far away from the minimum. This would mean that the H₂/CO ratio could not affect the $\Delta\mu_C$, and the carbon-rich facets would remain stable at very high H₂/CO ratio. Obviously, this disagrees with the experimental results, because high H₂ partial pressure will retard carbon deposition and even reduce iron carbide into metallic iron. Instead of using only single reaction to estimate the changes of the $\Delta\mu_C$, we combined different reactions. However, it should be noted that these independent reactions impose chemical force to the phase transition of catalysts and the extent of each reaction to carbon balance of the catalyst has not been well defined. Therefore, we supposed three different extents of each reaction and discuss these situations respectively

Scheme A: (2) + (3) + (7)



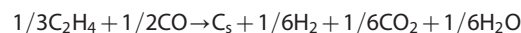
$$\mu_C = 3/4\mu_{CO} + 1/4\mu_{C_2H_4} - 1/4\mu_{H_2} - 1/4\mu_{H_2O} - 1/4\mu_{CO_2}$$

Scheme B: (2) \times 2 + (3) + (7)



$$\mu_C = \mu_{CO} + 1/5\mu_{C_2H_4} - 1/5\mu_{H_2} - 1/5\mu_{H_2O} - 2/5\mu_{CO_2}$$

Scheme C: (2) + (3) + (7) \times 2



$$\mu_C = 1/2\mu_{CO} - 1/3\mu_{C_2H_4} - 1/6\mu_{H_2} - 1/6\mu_{H_2O} - 1/6\mu_{CO_2}$$

In a typical Fe based FTS process, the most important parameters influencing the catalyst performance are the chemical composition of fluids surrounding the catalyst, temperature and pressure. In this study, the gas environment is designed in composition with CO + H₂ (varying H₂/CO ratio), $-CH_2-$ (light hydrocarbons), CO₂ and H₂O of 75, 10, 12 and 3%, respectively, representing the typical industrial conditions. Since we did not consider the contribution of the condensed heavy hydrocarbons and oxygenates, the ratios of carbon, oxygen and hydrogen are not stoichiometric. For comparison, we also included a gas phase free from CO with H₂ and hydrocarbons, which simulates the weaker carburization environment for the iron catalyst as tested in fundamental studies in FTS.⁶²

Under real CO involved environment, the influences of temperature and pressure on $\Delta\mu_C$ are evaluated for H₂/CO ratio of 2, 4 and 8 with other gas compositions presented in Table 3, and the main results are shown in Fig. 3. At a total pressure fixed at 30 atm (Fig. 3a), it is found that higher temperature leads to lower (more negative) $\Delta\mu_C$ for all three schemes with different H₂/CO ratios, in consistent with the results of de Smit *et al.*⁶³ At a given temperature the μ_C

determined in Scheme B is the highest, followed by those in Scheme A and Scheme C. This trend implies that CO has stronger carburization ability than C₂H₄.

Figure 3b shows the results with varying pressure at 550 K. For Scheme B and Scheme A, higher pressure leads to higher (less negative) $\Delta\mu_C$, which indicates lower pressure can retard carbon deposition. In the whole pressure range (1 to 60 atm), the $\Delta\mu_C$ determined by Scheme C keeps constant.

Figure 3c presents the H₂/CO ratio influence on $\Delta\mu_C$ at 550 K and 30 atm, with the gas composition presented in Table 4. As H₂/CO ratio increases from 1/1 to 20/1, the $\Delta\mu_C$ determined by all three schemes decreases and this implies that excess hydrogen would retard carbon deposition. However, it should be noted that even at extremely high H₂/CO ratio (20/1) $\Delta\mu_C$ does not become lower than the critical value for stable iron carbide phases, i.e. -7.83 eV for ϵ -Fe₂C, -7.80 eV for χ -Fe₅C₂ and θ -Fe₃C as well as -8.01 eV for Fe₄C. This reveals the thermodynamic possibility for carbon deposition at very high H₂/CO ratios beyond stable iron carbide phases under extended FTS operation conditions. Such carbon deposition destroys the mechanical structure of catalysts as observed in industrial practices and deactivates the catalysts.⁵⁷ It is noted that the same trends in Schemes A–C have been found for using CH₄ as light hydrocarbon model (Supplementary Material).

How to keep the activity of the catalysts by adjusting the chemical and physical parameters remains to be a headache problem and challenging. Rising temperature can retard carbon deposition thermodynamically, but accelerate carburization kinetically. Lowering pressure is thermodynamically and kinetically promising, but reduces significantly the process productivity. Increasing H₂/CO ratio is therefore a reasonable choice with thermodynamic and kinetic advantages as well as controllable process productivity. It should be noticed that our current calculations depend very strongly on three different carburization schemes that hopefully can cover all possibilities in real FTS systems. The exact schemes should be determined by experimental studies, which show the chemical extents of different carbon formations steps, namely (2), (3) and (7) in Table 2. This should be done by experiments with well defined techniques and operation conditions. Such studies provide a precise thermodynamic basis for the fundamental investigation along with *ab initio* atomistic thermodynamics developed in this work.

In FTS reaction system, the influence of CO₂ and H₂O contents on the $\Delta\mu_C$ is presented in Fig. 4, with the gas composition listed in Tables 5 and 6. It shows clearly that increasing the content of CO₂ (5 to 25%) and H₂O (1 to 15%) lowers $\Delta\mu_C$ at very low degree. The results indicate that CO₂

Table 3 Gas composition under H₂/CO ratios of 2, 4 and 8

H ₂ /CO	2	4	8
H ₂ (%)	50.00	60.00	66.67
CO (%)	25.00	15.00	8.33
CH ₄ (%)	10.00	10.00	10.00
CO ₂ (%)	12.00	12.00	12.00
H ₂ O (%)	3.00	3.00	3.00

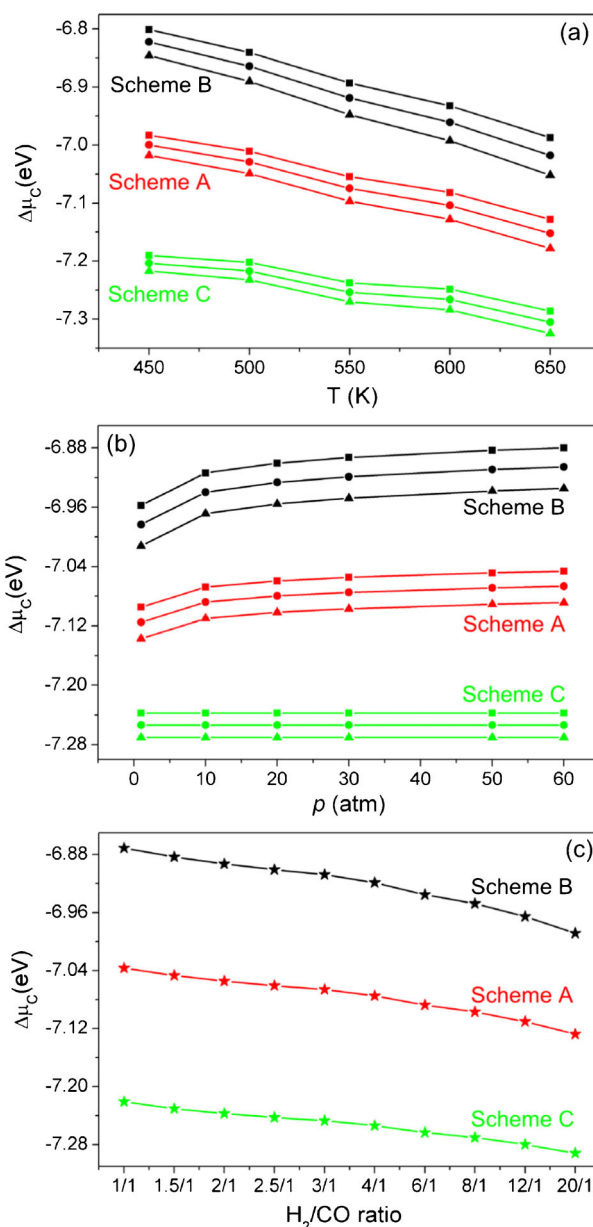


Figure 3 Relationship of carbon chemical potential ($\Delta\mu_C$) to **a** temperature (450–650 K) at 30 atm and H₂/CO ratio of 2, 4 and 8; **b** pressure (1–60 atm) at 550 K and H₂/CO ratio of 2, 4 and 8; **c** H₂/CO ratio (1 to 20) at 550 K and 30 atm (■ for H₂/CO=2; • for H₂/CO=4 and ▲ for H₂/CO=8)

Table 4 Gas composition under different H₂/CO ratios at 550 K and 30 atm

H ₂ /CO	H ₂ /%	CO/%	CH ₄ /%	CO ₂ /%	H ₂ O/%
1.0	37.50	37.50	10.00	12.00	3.00
1.5	45.00	30.00	10.00	12.00	3.00
2.0	50.00	25.00	10.00	12.00	3.00
2.5	53.57	21.43	10.00	12.00	3.00
3.0	56.25	18.75	10.00	12.00	3.00
4.0	60.00	15.00	10.00	12.00	3.00
6.0	64.29	10.71	10.00	12.00	3.00
8.0	66.67	8.33	10.00	12.00	3.00
12.0	69.23	5.77	10.00	12.00	3.00
20.0	71.43	3.57	10.00	12.00	3.00

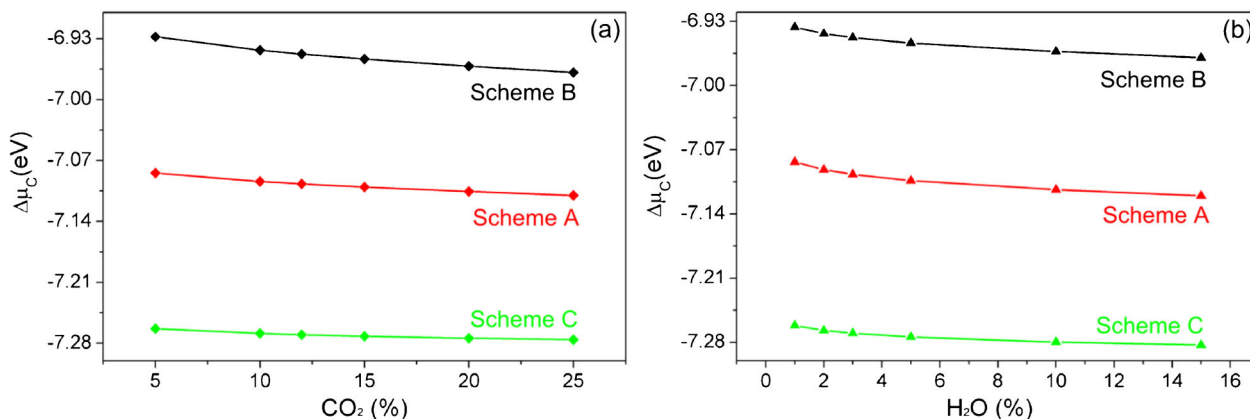


Figure 4 Relationship of carbon chemical potential ($\Delta\mu_C$) to **a** CO₂ content and **b** H₂O content at 550 K, 30 atm and H₂/CO=8

and H₂O, the byproduct in FTS, play only subordinate role in controlling phase transition process and should be removed from the process as usual (Fig. 1) for achieving other process benefits.

These compared results in Schemes A–C imply that we may use different unsaturated hydrocarbons and CO to optimize the environment for getting stable catalyst phases, especially for initializing the FTS process. It has been proved experimentally that unsaturated light hydrocarbons and H₂, instead of CO and H₂, can conduct chain growth reactions over iron based FTS catalysts.⁶² In order to conduct efficient FTS reactions it is necessary to optimize the carburization ability of the chemical–physical environments (temperature, pressure and H₂/CO ratio) in terms of μ_C . The insight behind μ_C is the change of the stable iron carbide phases as well as the surface structure and composition.

Surface stability

To get the equilibrium shapes of ε -Fe₂C, θ -Fe₃C and Fe₄C under different operation conditions, we studied both low and high Miller index facets of these carbides, which contain all low Miller index surfaces and the characteristic peaks in X-ray diffraction.^{37,64,65} All calculated surfaces and the equivalent Miller index are listed in the Supplementary Material (Table S3). Because of their complex bulk structures, each surface has several terminations (including both stoichiometric and non-stoichiometric terminations), e.g. five terminations for each of the (101), (102) and (103) surfaces of ε -Fe₂C; 16 terminations for each of the (111), (113), (133) and (131) surfaces of θ -Fe₃C; and each facet of Fe₄C has two terminations. Here we used the surface Fe/C ratio ($\alpha = n_{Fe}/n_C$) to distinguish these terminations as discussed previously.³⁰ In the following discussion, the number following the Miller index indicates the surface Fe/C ratio. The surface free

energies of these terminations within the $\Delta\mu_C$ range from -8.50 to -6.00 eV are given in the Supplementary Material (Fig. S3) for comparison, and only the results of the most stable termination of each facet are used for discussion.

Figures 5–7 show the relationship between surface free energy ($\gamma(T,p)$) of the most stable facets of ε -Fe₂C, θ -Fe₃C and Fe₄C and $\Delta\mu_C$. Similar to Fe₅C₂,³⁰ carbon-rich termination with lower α value becomes more stable at higher (less negative) $\Delta\mu_C$ for all iron carbides, while the carbon-poor terminations are more favorable at lower (more negative) $\Delta\mu_C$. With the increasing $\Delta\mu_C$, the most stable termination changes from carbon-poor (higher Fe/C ratio) to carbon-rich (lower Fe/C ratio), and the turn points represent the change of the stable termination and they differ from facet to facet. By combining theory and *in situ* XPS studies de Smit *et al.*⁶³ also found that body centered cubic Fe and surface/subsurface carbon are more stable at high temperature (low μ_C), while the carbon-rich χ -Fe₅C₂ (100) surface becomes thermodynamically more stable upon lowering the temperature (high μ_C). Since excessive carbon deposition will deactivate the catalysts and lower the catalytic performance,⁵⁷ avoiding carbon deposition can be improved by using proper temperature, pressure and gas environment.

For ε -Fe₂C (Fig. 5), (1 $\bar{2}$ 1)-2.00 and (101)-1.50 are the most stable facets, followed by (2 $\bar{2}$ 1)-2.67/1.33, and (0 $\bar{1}$ 1)-2.00/1.33. The least stable surfaces are (2 $\bar{0}$ 1)-2.67/1.33, and (103)-2.50/1.00. The other surfaces, (0 $\bar{1}$ 3)-2.67/1.50, (001)-4.00/1.00, (110)-2.00/1.33, (112)-2.00/1.00, (100)-2.00/1.00, (0 $\bar{1}$ 2)-4.00/1.00, (102)-4.00/2.00, (111)-3.00/1.33, have intermediate stability. It is also noted that for the (1 $\bar{2}$ 0), (010), (1 $\bar{2}$ 1) and (1 $\bar{2}$ 2) facets, the stoichiometric terminations are most stable (Fig. S3).

Table 5 Gas composition at 550 K and 30 atm with H₂/CO ratio of 8 for different CO₂ contents

CO ₂ /%	H ₂ /%	CO/%	CH ₄ /%	H ₂ O/%
5.00	72.89	9.11	10.00	3.00
10.00	68.44	8.56	10.00	3.00
12.00	66.67	8.33	10.00	3.00
15.00	64.00	8.00	10.00	3.00
20.00	59.56	7.44	10.00	3.00
25.00	55.11	6.89	10.00	3.00

Table 6 Gas composition at 550 K and 30 atm with H₂/CO ratio of for different H₂O contents

H ₂ O/%	H ₂ /%	CO/%	CH ₄ /%	CO ₂ /%
1.00	68.44	8.56	10.00	12.00
2.00	67.56	8.44	10.00	12.00
3.00	66.67	8.33	10.00	12.00
5.00	64.89	8.11	10.00	12.00
10.00	60.44	7.56	10.00	12.00
15.00	56.00	7.00	10.00	12.00

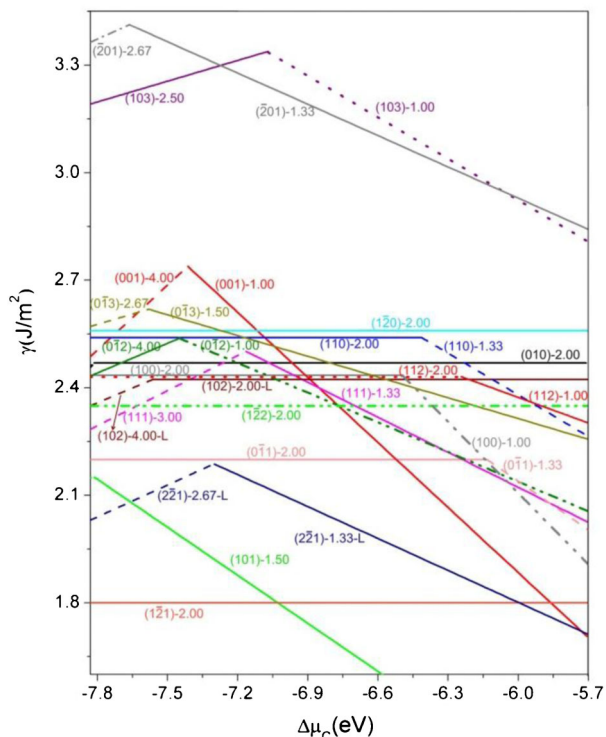


Figure 5 Relationship of surface free energies of most stable facets of ϵ -Fe₂C to $\Delta\mu_C$ (indices given in parentheses indicates corresponding Miller index, and second term of indices provides corresponding surface α =Fe/C ratio)

For θ -Fe₃C (Fig. 6), (010)-2.33 is the most stable one. The least stable surface is (100) with α =2.50 or 2.00. The other surfaces, (110)-3.00/2.33, (133)-2.67/2.40/2.33, (113)-2.80/2.40, (131)-2.50, (102)-3.00/2.40, (011)-3.00/2.00, (001)-3.00/2.00, (101)-2.25/2.00, (111)-2.00, (031)-3.00/2.00, have intermediate stability.

For Fe₄C (Fig. 7), (100) with α =3.00 is the most stable facet. The surface free energies of other facets are significantly higher than (100), and the least stable surface is (133)-6.00/3.00, followed by (110)-3.00, (111)-4.00/2.00, (131)-6.00/2.67 and (210)-5.00/3.33, have intermediate stability.

For Fe₅C₂³⁰ as reported previously, the (100) termination is most stable with α =2.25, followed by (111)-2.17/1.75, (510)-2.50, and (110)-2.40/2.00. The least stable surfaces are (10 $\bar{1}$)-2.75/2.25, (001)-2.50; (11 $\bar{3}$)-2.50, (113)-2.00 and (101)-1.50. In addition, (110)-2.40/2.00, (010)-2.50; (133)-1.75; (11 $\bar{1}$)-2.50, (511)-2.25, (221)-3.00, ($\bar{4}$ 11)-2.50, (011)-2.40/2.20 have stability in between.

Crystallite morphology

In order to estimate the crystallite morphology of these iron carbides, it is necessary to determine the equilibrium crystal shape by using the standard Wulff construction.⁶⁶ In the standard Wulff construction, the surface free energy for a given closed volume is minimized and the exposure of a facet depends not only on surface free energy but also on orientation in crystal.⁶⁷ Since the surface free energy of each facet is a function of μ_C , the crystal shape should also be a function of the $\Delta\mu_C$ that corresponds to different experimental conditions of temperature, pressure and atmosphere. Figure 8 presents the morphology of the ϵ -Fe₂C, θ -Fe₃C and Fe₄C crystals at different $\Delta\mu_C$, corresponding to different gas

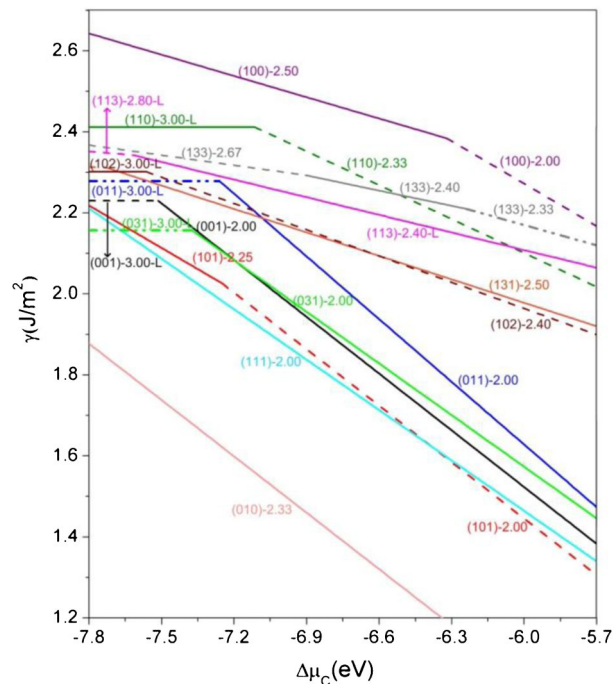


Figure 6 Relationship of surface free energies of most stable facets of θ -Fe₃C to $\Delta\mu_C$ (indices given in parentheses indicates corresponding Miller index, and second term of indices provides corresponding surface α =Fe/C ratio)

compositions at 550 K and 30 atm, respectively, along with that of χ -Fe₅C₂ (slightly modified form compared to our previous report, where an incorrect default crystal parameter was used; however, this does not affect our conclusion). The proportions of exposed terminations of ϵ -Fe₂C, χ -Fe₅C₂ and θ -Fe₃C are listed in Tables 7, 8 and 9.

At lower $\Delta\mu_C$ (-7.60 eV), the crystallite of ϵ -Fe₂C has 11 exposed surface terminations in different Fe/C ratios, (100), (010), (001), (101), (0 $\bar{1}$ 1), (110), (111), (1 $\bar{1}$ 1), (102), (0 $\bar{1}$ 2) and (2 $\bar{2}$ 1). The (1 $\bar{1}$ 1) termination has the largest portion (35.3%) of the surface area, followed by the (101) and (2 $\bar{2}$ 1) terminations (27.7 and 16.7%, respectively), and they cover about 80% of the total surface area of the crystal. As the $\Delta\mu_C$ increases to -7.10 eV, (0 $\bar{1}$ 1), (001) and (102) are

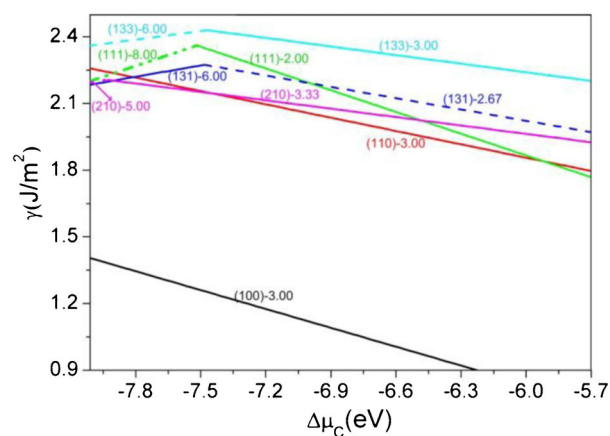


Figure 7 Relationship of surface free energies of most stable facets of Fe₄C to $\Delta\mu_C$ (indices given in parentheses indicates corresponding Miller index, and second term of indices provides corresponding surface α =Fe/C ratio)

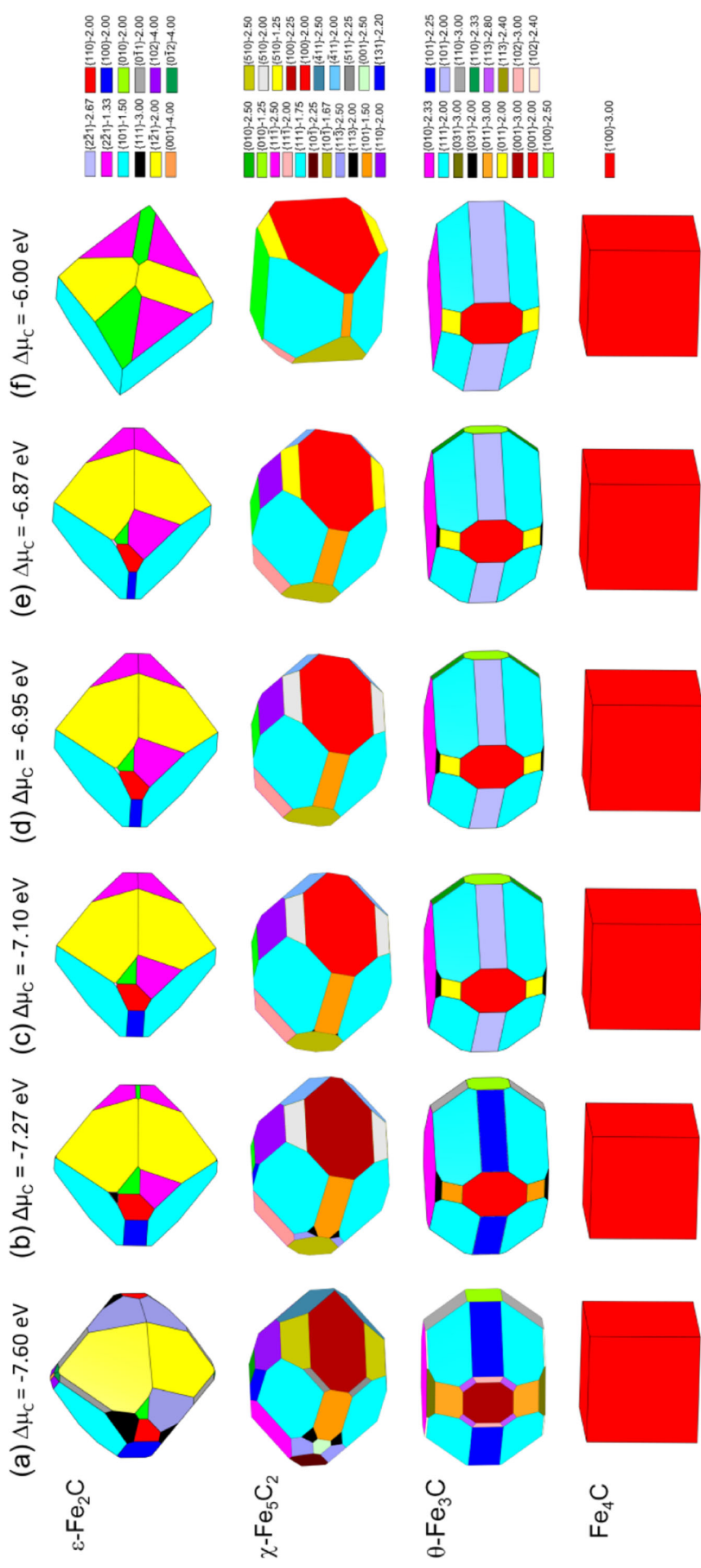


Figure 8 Morphologies of ϵ -Fe₂C, χ -Fe₅C₂, θ -Fe₃C and Fe₄C at different μ_C at 550 K and 30 atm: a for C₂H₄ (15%) condition; b for Scheme C with H₂/CO=8.0; c for Scheme A with H₂/CO=8.0; d for Scheme B with H₂/CO=8.0; e for C₂H₂ (15%) condition. Indices given in legend indicates corresponding Miller index, and second term of indices provides corresponding surface α =Fe/C ratio)

disappeared, and the carbon-rich ($2\bar{2}1$)-1.33 termination becomes more stable than the carbon-poor ($2\bar{2}1$)-2.67 termination. As the $\Delta\mu_C$ increases, the proportion of (100), (111), ($1\bar{2}1$) and ($0\bar{1}2$) decreases, while the area of (101) and (010) increases. When the $\Delta\mu_C$ reaches to -6.0 eV, the

crystallite of ε -Fe₂C has only four exposed surface terminations and they are (101), ($1\bar{2}1$), (010) and ($2\bar{2}1$). The (101) becomes the largest exposed surface (59.5%), and the facets ($1\bar{2}1$), (101) and ($2\bar{2}1$) still cover the most surface area (92%) of the crystal.

Table 7 Facets contributions (%) to total surface area in Wulff construction of ε -Fe₂C presented in Fig. 8

Facet	(a) C ₂ H ₄	(b) Scheme C	(c) Scheme A	(d) Scheme B	(e) C ₂ H ₂	(f) $\Delta\mu_C = -6.0$ eV
(100)-2.00	5.52	3.74	2.75	1.85	1.36	0.00
(010)-2.00	0.55	1.45	0.86	0.64	0.53	7.99
(001)-1.00	0.18	0.00	0.00	0.00	0.00	0.00
(101)-1.50	27.70	40.81	44.13	46.96	48.52	59.52
($0\bar{1}1$)-2.00	4.14	0.00	0.00	0.00	0.00	0.00
(110)-2.00	3.43	4.96	3.96	3.01	2.51	0.00
(111)-1.33	0.03	0.06	0.07	0.00
(111)-3.00	4.91	0.28
($1\bar{2}1$)-2.00	35.25	39.02	36.41	34.15	32.93	17.32
(102)-2.00	0.97	0.00	0.00	0.00	0.00	0.00
($0\bar{1}2$)-1.00	0.65	0.03	0.00	0.00	0.00	0.00
($2\bar{2}1$)-1.33	...	9.70	11.85	13.34	14.09	15.18
($2\bar{2}1$)-2.67	16.71

Table 8 Facets contributions (%) to total surface area in Wulff construction of χ -Fe₅C₂ presented in Fig. 8

Facet	(a) C ₂ H ₄	(b) Scheme C	(c) Scheme A	(d) Scheme B	(e) C ₂ H ₂	(f) $\Delta\mu_C = -6.0$ eV
(010)-2.50	1.20
(010)-1.25	...	0.92	2.06	2.83	3.33	10.44
($11\bar{1}$)-2.50	11.72
($11\bar{1}$)-2.00	...	9.76	9.42	9.06	8.91	2.25
(001)-2.50	0.92	0.00	0.00	0.00	0.00	0.00
(510)-2.50	9.58
(510)-2.00	...	6.38	5.79	6.05
(510)-1.25	6.25	5.37
(113)-2.00	0.91	0.35	0.03	0.00	0.00	0.00
($\bar{4}11$)-2.50	9.14
($\bar{4}11$)-2.00	...	6.35	4.56	2.74	1.87	0.00
($11\bar{3}$)-2.50	3.33	1.02	0.00	0.00	0.00	0.00
(101)-1.50	4.53	4.92	4.65	4.24	4.00	1.42
(100)-2.25	16.63	20.24
(100)-2.00	21.67	23.07	23.76	31.84
(110)-2.00	10.49	12.90	11.87	10.54	9.64	0.00
(111)-1.75	23.81	30.41	32.60	33.65	34.22	39.99
(511)-2.25	1.19	0.00	0.00	0.00	0.00	0.00
(131)-2.20	3.34	0.68	0.20	0.00	0.00	0.00
($10\bar{1}$)-2.25	3.21
($10\bar{1}$)-1.67	...	6.07	7.35	7.82	8.02	8.69

Table 9 Facets contributions (%) to total surface area in Wulff construction of θ -Fe₃C presented in Fig. 8

	(a) C ₂ H ₄	(b) Scheme C	(c) Scheme A	(d) Scheme B	(e) C ₂ H ₂	(f) $\Delta\mu_C = -6.0$ eV
(001)-3.00	5.03
(001)-2.00	...	6.80	6.82	6.82	6.79	6.81
(010)-2.33	20.31	23.94	24.74	25.44	25.77	29.99
(100)-2.50	3.46	3.36	3.06	2.53	2.24	0.00
(101)-2.25	13.25	12.60
(101)-2.00	13.06	13.89	14.49	21.39
(110)-3.00	9.28	4.96
(110)-2.33	3.04	2.38	2.04	0.00
(011)-3.00	5.60	2.36
(011)-2.00	2.28	2.42	2.50	2.92
(111)-2.00	35.88	44.38	45.75	45.63	45.45	38.88
(113)-2.80	1.21
(113)-2.40	...	0.00	0.00	0.00	0.00	0.00
(031)-3.00	3.92
(031)-2.00	...	1.61	1.25	0.89	0.71	0.00
(102)-3.00	0.85
(102)-2.40	...	0.00	0.00	0.00	0.00	0.00

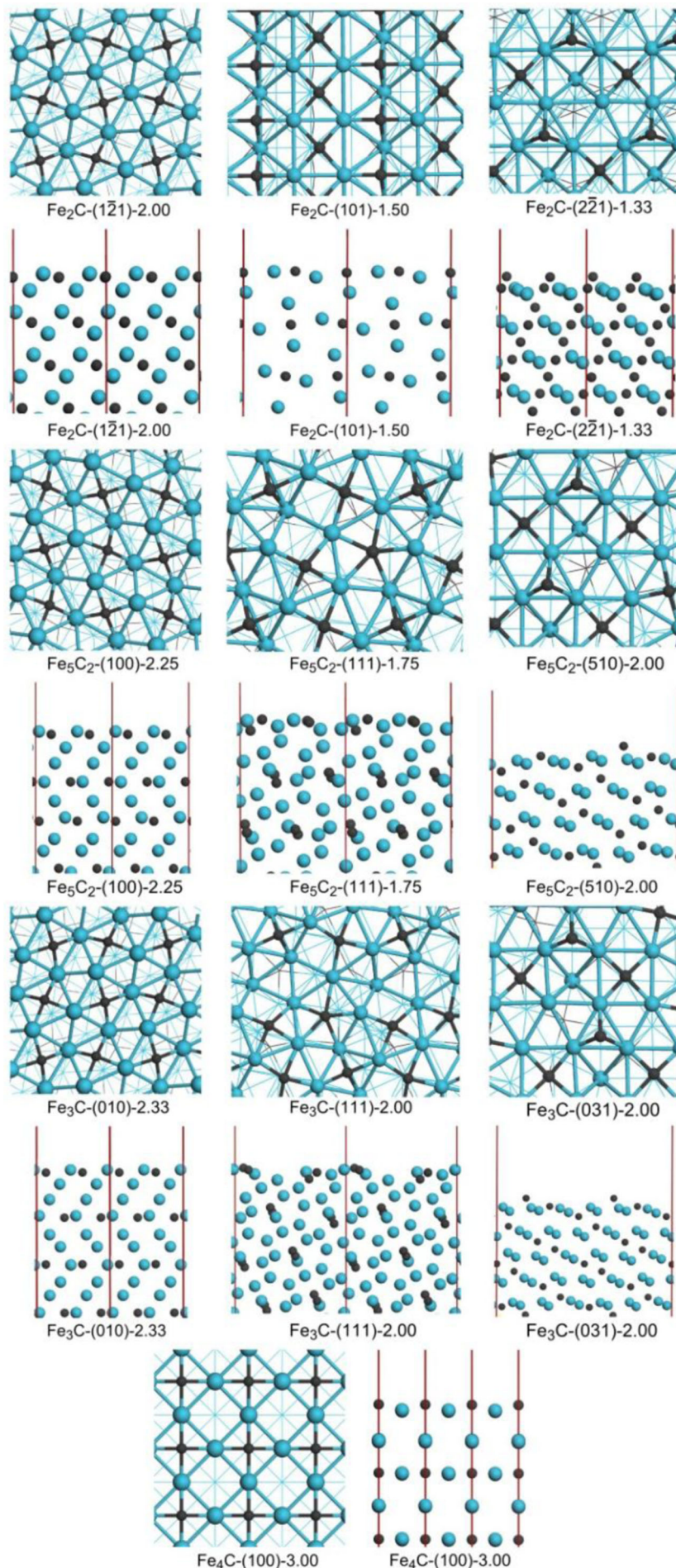


Figure 9 Surface structures of most stable surfaces and surfaces that have largest exposed surface area in Wulff construction of ϵ -Fe₂C, χ -Fe₅C₂, θ -Fe₃C and Fe₄C (indices given in parentheses indicates corresponding Miller index, and the third term of the indices provides the corresponding surface α =Fe/C ratio, Fe atoms are shown by blue balls, C atoms are shown by black balls)

At lower $\Delta\mu_C$ (−7.60 eV), the crystallite of χ -Fe₅C₂ has 14 exposed surface terminations in different Fe/C ratios, (010), (11 $\bar{1}$), (001), (510), (113), ($\bar{4}$ 11), (11 $\bar{3}$), (101), (100), (110), (111), (511), (131) and (10 $\bar{1}$). The (111), (100) and (11 $\bar{1}$) surfaces cover 52.1% of the total surface area of the crystal (23.8, 16.6 and 11.7%, respectively). When the $\Delta\mu_C$ increases to −6.95 eV, the facets (001), (511), (113), (11 $\bar{3}$), and (131) are disappeared, and the carbon-rich termination of (010), (11 $\bar{1}$), (10 $\bar{1}$), (510), ($\bar{4}$ 11) and (100) are exposed. As the $\Delta\mu_C$ increases, the proportion of (100), (010), (111) and (10 $\bar{1}$) increases, while the exposed areas of all the other surfaces decrease. At higher $\Delta\mu_C$ (−6.00 eV), only seven facets are still exposed, among which the (111) and (100) terminations cover as much as 71.8% of the surface area of the crystal.

When the $\Delta\mu_C$ is −7.60 eV, the crystallite of θ -Fe₃C has 11 exposed surface terminations, (001), (100), (010), (101), (110), (011), (111), (113), (131), (102) and (031). The (111) facet has the largest portion of the total surface area (35.9%), followed by the (010) (20.3%) and (101) (13.3%) facets. As the $\Delta\mu_C$ increases to −6.95 eV, the proportions of (111) and (010) increase to 45.6 and 25.4%, respectively. The carbon-rich (031), (011), (001), (101) and (110) terminations are exposed under higher $\Delta\mu_C$ compared with lower μ_C . There are five facets still exposed at higher $\Delta\mu_C$ (−6.00 eV), among them the (111), (010) and (101) terminations cover 90.3% of the total surface area of the crystal (38.9, 30.0 and 21.4%, respectively).

In the whole range of $\Delta\mu_C$ that we considered, the crystallite of Fe₄C only exposes the (100)-3.00 termination.

Surface property

In the most stable terminations of each iron carbides (Fig. 9), ϵ -Fe₂C-(1 $\bar{2}$ 1)-2.00, χ -Fe₅C₂-(100)-2.25, θ -Fe₃C-(010)-2.33 and Fe₄C-(100)-3.00, each surface carbon atom coordinates with four surface iron atoms, and each surface iron atom coordinates with two surface carbon atoms. In addition, the most exposed surfaces, χ -Fe₅C₂-(111)-1.75 and θ -Fe₃C-(111)-2.00, have similar atom arrangement on partial surface structures. The third exposed facet of ϵ -Fe₂C, (2 $\bar{2}$ 1)-1.33, has also some similar surface structure with χ -Fe₅C₂-(510)-2.00 as

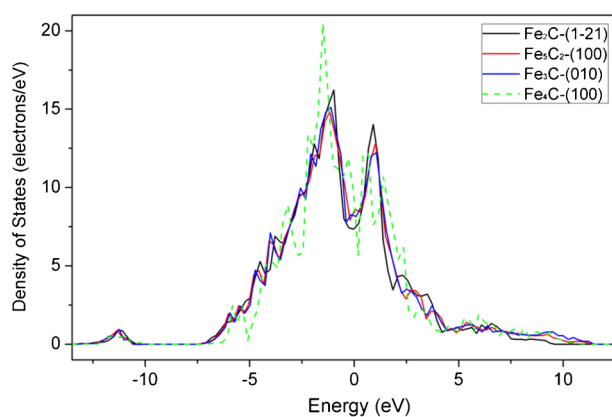


Figure 10 Density of states of surface layer atoms of most stable facets

well as θ -Fe₃C-(031)-2.00. The computed density of states of the surface layer atoms (Fig. 10) also revealed the similarity of these surface structures.

Since the pattern and density of carbonaceous deposit on surface can significantly influence the catalytic performance,^{68,69} similar and unique catalytic activities of the carbides facets with the same atom arrangement on surface layer should be expected. At first we analyzed the surface properties, e.g. the charge and binding energy of the surface carbon atoms, as well as the surface work function (difference between the electrostatic potential energy in the vacuum region and the Fermi energy of the slab), which is an important electronic indicator of a surface, i.e. lower work function indicates the higher electron donating ability of the surface. In addition, we also computed the adsorption structure and energy of CO on these surfaces. As shown in Fig. 11, the most stable CO adsorption site is the Fe-top site

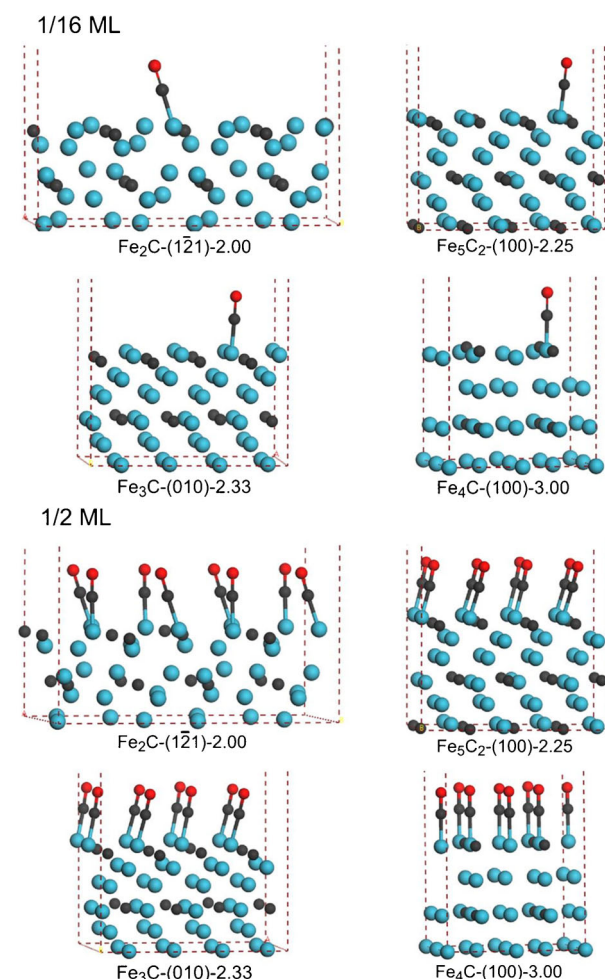


Figure 11 Adsorption of CO on most stable facet of ϵ -Fe₂C, χ -Fe₅C₂, θ -Fe₃C and Fe₄C with different coverage (indices given in parentheses indicates corresponding Miller index, and third term of indices provides corresponding surface α =Fe/C ratio, Fe atoms in blue, C atoms in black and O atoms in red)

on the ε -Fe₂C-(1 $\bar{1}21$)-2.00, χ -Fe₅C₂-(100)-2.25 and θ -Fe₃C-(010)-2.33 surfaces. The Fe₄C-(100)-3.00 facet has hollow site on the surface, the most stable CO adsorption site is the 4-fold site. In order to compare with other three carbides, the less stable Fe-top site of CO adsorption is taken into account (adsorption energy of CO on the Fe-top site is only 0.054 eV higher than that of the 4-fold site).

At 1/16 and 1/2 ML (Table 10), as the surface work function increases in the order of χ -Fe₅C₂-(100)-2.25 < θ -Fe₃C-(010)-2.33 < ε -Fe₂C-(1 $\bar{1}21$)-2.00 < Fe₄C-(100)-3.00, both CO adsorption energies and C-O bond elongation as well as the net negative charge of the adsorbed CO molecules decrease, implying that CO favors to adsorb on the surface with lower work function. Consequently, the χ -Fe₅C₂-(100)-2.25 has the largest CO adsorption energy, followed by θ -Fe₃C-(010)-2.33, ε -Fe₂C-(1 $\bar{1}21$)-2.00 and Fe₄C-(100)-3.00, respectively. The C-O bond activation degree is almost the same on χ -Fe₅C₂-(100)-2.25, θ -Fe₃C-(010)-2.33 and ε -Fe₂C-(1 $\bar{1}21$)-2.00, while Fe₄C-(100)-3.00 has the weakest ability to activate the C-O bond. For each surface, when the coverage of CO increases from 1/16 to 1/2 ML, both CO adsorption energies and C-O bond elongation decrease.

On the basis of the computed binding energy of surface carbon atoms, it is evident that less negatively charged surface carbon atoms have weaker bonding to the surface. Since CH₄ formation energy exhibits a linear relationship with the charge of surface carbon atom,²⁴ one can expect that CH₄ formation is most favored thermodynamically on χ -Fe₅C₂-(100)-2.25, followed by θ -Fe₃C-(010)-2.33, ε -Fe₂C-(1 $\bar{1}21$)-2.00 and Fe₄C-(100)-3.00.

Conclusion

In this work, we employed DFT calculations and *ab initio* atomistic thermodynamics to investigate the surface structure and stability of the low and high Miller index surfaces of the ε -Fe₂C, χ -Fe₅C₂, θ -Fe₃C and Fe₄C phases as well as their crystal shapes. The goal is to understand the effects of the FTS conditions on the structure and stability of iron carbides as FTS catalysts as well as their differences in surface properties.

The chemical-physical environment around iron based FTS catalysts under working conditions is described from thermodynamic aspect. With different carbon containing gas environments under real FTS operating conditions, it is found that the carburization ability depends mainly on the carbon content of the gas environments, i.e. the higher carbon content of C containing gases, the higher the carburization ability. It is also found that higher temperature, lower pressure and higher H₂/CO ratio can suppress carburization ability and retard carbon deposition.

The crystal shapes of ε -Fe₂C, χ -Fe₅C₂, θ -Fe₃C and Fe₄C have been determined by using the standard Wulff construction on the basis of the calculated surface free energies. Under different pretreatment conditions, the surface morphologies of ε -Fe₂C, χ -Fe₅C₂ and θ -Fe₃C are different in termination and proportion of each facet area, and the most stable non-stoichiometric termination changes from carbon-poor to carbon-rich (varying surface Fe/C ratio) upon the increase in $\Delta\mu_C$. The surface structure and composition of the most stable terminations have similar atom arrangement on the surface layer and the catalytic activities of these facets have been investigated. It is found that lower work function of the surface leads to larger adsorption energy of CO. Less negatively charged surface carbon atoms have weaker binding energy on the surface. Among these four carbides, χ -Fe₅C₂-(100)-2.25 is most favored for CO adsorption and CH₄ formation, followed by θ -Fe₃C-(010)-2.33, ε -Fe₂C-(1 $\bar{1}21$)-2.00 and Fe₄C-(100)-3.00, respectively. The activation degree of C-O bonds are almost same on χ -Fe₅C₂-(100)-2.25, θ -Fe₃C-(010)-2.33 and ε -Fe₂C-(1 $\bar{1}21$)-2.00, while Fe₄C-(100)-3.00 has the weakest ability for activating the C-O bond.

Appendix

Configuration modeling of fractional site occupancy in ε -Fe₂C

Figure A1 shows the unit cell structure of ε -Fe₂C, and this unit cell has the occupancy of carbon atoms of only 0.5

Table 10 Calculated adsorption energies (E_{ads} , eV) per CO, bond lengths (d , Å), net charges (q , e) and CO stretching frequencies (ν , cm⁻¹) on carbide surfaces, as well as surface properties of each facet

	χ -Fe ₅ C ₂	θ -Fe ₃ C	ε -Fe ₂ C	Fe ₄ C
Surface	(100)-2.25	(010)-2.33	(1 $\bar{1}21$)-2.00	(100)-3.00
Work function/eV	3.847	3.991	4.009	4.713
$q^*(C_s)$	-1.062	-1.090	-1.098	-1.119
$E_{\text{ads}}(C_s)$	-8.442	-8.459	-8.580	-9.126
$E_{\text{ads}}(1/16 \text{ ML})^\dagger$	-1.464	-1.442	-1.345	-0.946
$E_{\text{ads}}(1/16 \text{ ML})^\ddagger$	-1.741	-1.719	-1.667	-1.263
$d(\text{C-O})$ (1/16 ML)	1.171	1.172	1.170	1.164
$q^*(\text{CO})$ (1/16 ML)	-0.273	-0.277	-0.254	-0.226
ν_{CO} (1/16 ML)	1937	1933	1939	1990
$E_{\text{ads}}(1/2 \text{ ML})^\dagger$	-1.142	-1.135	-1.133	-0.317
$E_{\text{ads}}(1/2 \text{ ML})^\ddagger$	-1.482	-1.483	-1.489	-0.758
$d(\text{C-O})$ (1/2 ML)	1.162	1.163	1.163	1.159
$q^*(\text{CO})$ (1/2 ML)	-0.179	-0.176	-0.178	-0.091
ν_{CO} (1/2 ML)	1976	1971	1973	2017

*From Bader charge analysis.

†RPBE energies

‡PBE energies.

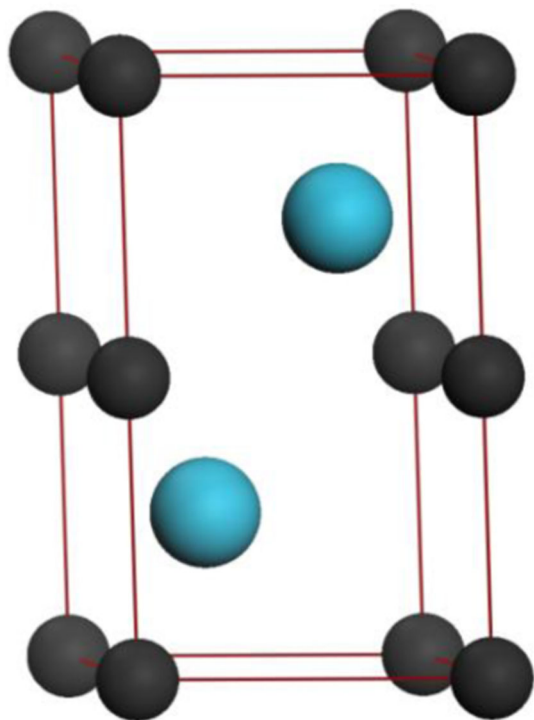


Figure A1 Unit cell structure of ϵ -Fe₂C (Fe atoms in blue balls, C atoms in black balls)

instead 1.0. This means that Fe atoms form a hexagonal close packed array and half of the octahedral interstitial sites are occupied by carbon atoms in a random way. Similar site-occupancy disorder structures are also found in β -Mo₂C⁷⁰ and Fe₂N.⁷¹ According to this bulk structure, the Fe/C ratio is 1 to 1. In order to keep the 2 to 1 stoichiometry, the usually used practice is to delete half of carbon atoms from the bulk structure. However, it will generate several configurations and the number of the possible configurations increases dramatically with the supercell size. Since there are no systematic investigations into the bulk structure of ϵ -Fe₂C known, several structures of ϵ -Fe₂C were used in previous studies. Jack reported a ϵ -Fe₂C structure by deleting carbon atoms on the vertices of the unit cell (Fig. A1).⁷² Jang *et al.*¹⁷ and Fang *et al.*¹⁸ calculated the ϵ -Fe₂C bulk structure with the space group *P*6₃22, which is different from the experimental data (*P*63/*mmc*).³⁷ In this work, we used the unit cell of ϵ -Fe₂C with the space group *P*63/*mmc* to generate the supercell by deleting half of the carbon atoms from the supercell. For supercell with different size, we calculated all possible structures in order to give a reasonable configuration of ϵ -Fe₂C.

Firstly, we generated the $2 \times 2 \times 1$ and $2 \times 2 \times 2$ supercells by deleting half of the carbon atoms from these

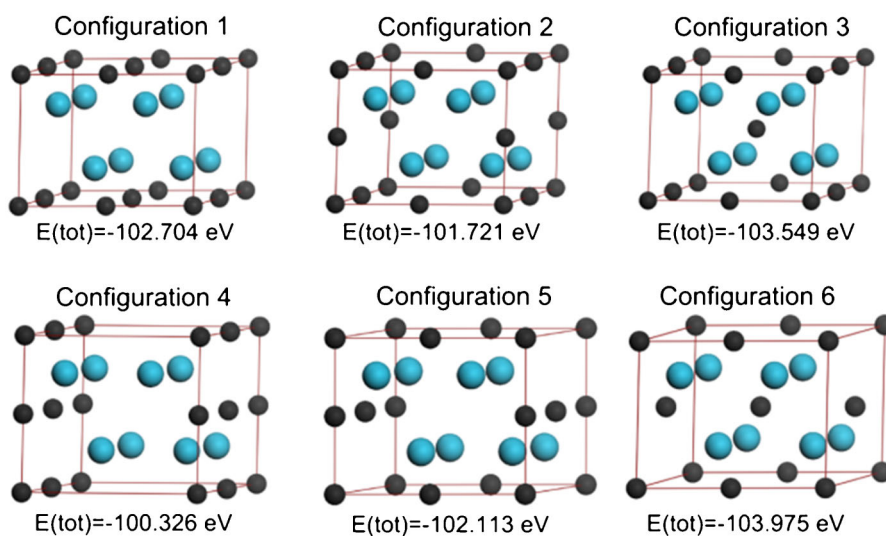


Figure A2 Optimized structures of $2 \times 2 \times 1$ supercell of ϵ -Fe₂C (Fe atoms in blue balls, C atoms in black balls)

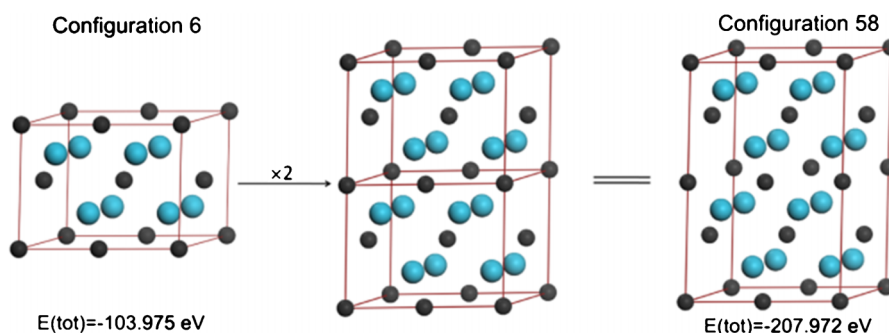


Figure A3 Optimized structures of $2 \times 2 \times 2$ supercell of ϵ -Fe₂C (Fe atoms are shown by blue balls, C atoms are shown by black balls)

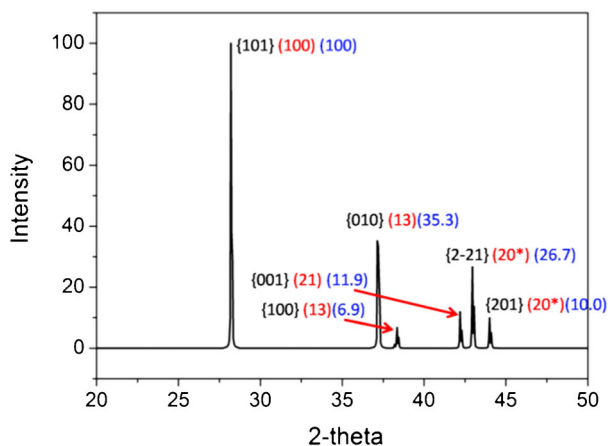


Figure A4 X-ray diffraction of ϵ -Fe₂C (detected intensities in red and calculated intensities in blue)

two structures. During this process, the site-occupancy disorder program was used to obtain all the supercell structures.⁷³ By taking the advantage of isometric transformation, site-occupancy disorder excludes the equivalent configurations and reduces the configurations only to the independent ones (Table A1). All the energies were obtained using the method described in the section on 'Structure calculation'. The occurrence probability of each configuration at temperature T can be obtained from equation (9)

$$P_n = \frac{1}{Z} \exp(-E_n/k_B T) \quad (9)$$

where $k_B = 8.6173 \times 10^{-5}$ eV K⁻¹, E_n is the energy of that configuration and

$$Z = \sum_{n=1}^N \exp(-E_n/k_B T) \quad (10)$$

The $2 \times 2 \times 1$ supercell has six independent configurations; the optimized structures and the corresponding total energies are shown in Fig. A2. Among these six structures, configuration 6 is most stable and its occurrence probability is 100% from 0 to 1000 K. After optimizing all 128 configurations of the $2 \times 2 \times 2$ supercell, we found configuration 58 to be most stable (Fig. A3). Its occurrence probability is also 100% from 0 to 1000 K. In addition, configuration 58 is two times of configuration 6, therefore they are the same structure. The simulated XRD spectrum is presented in Fig. A4, the relative intensity of the characteristic peaks agrees well with the experimental data.^{37,74} This rationalizes our calculated structure of ϵ -Fe₂C.

Table A1 Number of independent configurations for a series of supercell of ϵ -Fe₂C

Supercell	N ₀ [*]	N [†]	M [‡]
2 × 2 × 1	96	70	6
2 × 2 × 2	192	12,870	122

*Number of symmetry operations.

†Total number of configurations.

‡Number of independent configurations.

Conflicts of interest

The authors declare no conflicts of interest.

Acknowledgements

This work was supported by National Natural Science Foundation of China (Grant No. 21273261), National Basic Research Program of China (Grant No. 2011CB201406), and Chinese Academy of Science and Synfuels China Co., Ltd.

Supporting Information Available: The atomic thermodynamic method used for calculating surface free energies and the calculated surface free energies are available. This material is available free of charge via the Internet at <http://www.publicationethics.org>.

References

- F. Fischer and H. Tropsch: *Brennstoff-Chem.*, 1923, **4**, 276–285.
- F. H. Herbstein, J. Smuts and J. N. van Niekerk: *Anal. Chem.*, 1960, **32**, 20–24.
- E. de Smit, F. Xinquini, A. M. Beale, O. V. Safonova, W. van Beek, P. Sautet and B. M. Weckhuysen: *J. Am. Chem. Soc.*, 2010, **132**, 14928–14941.
- E. de Smit, I. Swart, J. F. Creemer, G. H. Hoveling, M. K. Gilles, T. Tyliczszak, P. J. Kooyman, H. W. Zandbergen, C. Morin, B. M. Weckhuysen and F. M. F. de Groot: *Nature*, 2008, **456**, 222–226.
- A. M. Datye, Y. Jin, L. Mansker, R. T. Motjope, T. H. Dlamini and N. J. Coville: *Stud. Surf. Sci. Catal.*, 2000, **130**, 1139–1144.
- A. Königer, C. Hammerl, M. Zeitler and B. Rauschenbach: *Phys. Rev. B*, 1997, **55B**, 8143–8147.
- D. L. Williamson, K. Nakazawa and G. A. Krauss: *Metall. Trans. A*, 1979, **10A**, 1351–1363.
- M. Manes, A. D. Damick, M. Mentser, E. M. Cohn and L. J. E. Hofer: *J. Am. Chem. Soc.*, 1952, **74**, 6207–6209.
- E. M. Cohn and L. J. E. Hofer: *J. Chem. Phys.*, 1953, **21**, 354–359.
- J. F. Shultz, W. K. Hall, T. A. Dubs and R. B. Anderson: *J. Am. Chem. Soc.*, 1955, **77**, 282–285.
- L. J. E. Hofer and E. M. Cohn: *Nature* 1951, **167**, 977–978.
- S. Nagakura: *J. Phys. Soc. Jpn*, 1959, **14**, 186–195.
- H. Merkel and F. Weinrotter: *Brennstoff-Chem.*, 1951, **32**, 289–297.
- W. C. Chiou Jr and E. A. Carter: *Surf. Sci.*, 2003, **530**, 88–100.
- D. C. Sorescu: *J. Phys. Chem. C*, 2009, **113C**, 9256–9274.
- Z. Q. Lv, S. H. Sun, P. Jiang, B. Z. Wang and W. T. Fu: *Comput. Mater. Sci.*, 2008, **42**, 692–697.
- J. H. Jang, I. G. Kim and H. K. D. H. Bhadeshia: *Scr. Mater.*, 2010, **63**, 121–123.
- C. M. Fang, M. A. van Huis and H. W. Zandbergen: *Scr. Mater.*, 2010, **63**, 418–421.
- H. I. Faraoun, Y. D. Zhang, C. Esling and H. Aourag: *J. Appl. Phys.*, 2006, **99**, 093508–093515.
- C. Jiang, S. G. Srinivasan, A. Caro and S. A. Maloy: *J. Appl. Phys.*, 2008, **103**, 043502–043509.
- B. Hallstedt, D. Djurovic, J. von Appen, R. Dronskowski, A. Dick, F. Körmann, T. Hickel and J. Neugebauer: *CALPHAD: Comput. Coupling Phase Diagr. Thermochem.*, 2010, **34**, 129–133.
- C. K. Ande and M. H. F. Sluiter: *Metall. Mater. Trans. A*, 2012, **43A**, 4436–4444.
- L. J. Deng, C. F. Huo, X. W. Liu, X. H. Zhao, Y. W. Li, J. G. Wang and H. J. Jiao: *J. Phys. Chem. C*, 2010, **114C**, 21585–21592.
- C. F. Huo, Y. W. Li, J. G. Wang and H. J. Jiao: *J. Am. Chem. Soc.*, 2009, **131**, 14713–14721.
- X. Y. Liao, D. B. Cao, S. G. Wang, Z. Y. Ma, Y. W. Li, J. G. Wang and H. J. Jiao: *J. Mol. Catal. A: Chem.*, 2007, **269**, 169–178.
- X. Y. Liao, S. G. Wang, Z. Y. Ma, Y. W. Li, J. G. Wang and H. J. Jiao: *J. Mol. Catal. A: Chem.*, 2008, **292**, 14–20.
- B. Q. Wei, M. Shima, R. Pati, S. K. Nayak, D. J. Singh, R. Ma, Y. Li, Y. Bando, S. Nasu and P. M. Ajayan: *Small*, 2006, **6**, 804–809.
- C. M. Deng, C. F. Huo, L. L. Bao, X. R. Shi, Y. W. Li, J. G. Wang and H. J. Jiao: *Chem. Phys. Lett.*, 2007, **448**, 83–87.
- C. M. Deng, C. F. Huo, L. L. Bao, G. Feng, Y. W. Li, J. G. Wang and H. J. Jiao: *J. Phys. Chem. C*, 2008, **112C**, 19018–19029.
- S. Zhao, X. W. Liu, C. F. Huo, Y. W. Li, J. G. Wang and H. J. Jiao: *J. Catal.*, 2011, **294**, 47–53.
- G. Kresse and J. Furthmüller: *Comput. Mater. Sci.* 1996, **6**, 15–50.
- G. Kresse and J. Furthmüller: *J. Phys. Rev. B*, 1996, **54B**, 11169–11186.

33. J. P. Perdew, K. Burke and M. Ernzerhof: *Phys. Rev. Lett.* 1996, **77**, 3865–3868.
34. P. E. Blochl: *Phys. Rev. B*, 1994, **50B**, 17953–17979.
35. G. Kresse: *Phys. Rev. B*, 1999, **59B**, 1758–1775.
36. M. Methfessel and A. T. Paxton: *Phys. Rev. B*, 1989, **40B**, 3616–3621.
37. G. H. Barton and B. Gale: *Acta Cryst.*, 1964, **17**, 1460–1462.
38. I. G. Wood, L. Vocadlo, K. S. Knight, D. P. Dobson, W. G. Marshall, G. D. Price and J. Brodholt: *J. Appl. Cryst.*, 2004, **37**, 82–90.
39. A. V. dos Santos, M. I. da Costa and C. A. Kuhnen: *J. Magn. Magn. Mater.*, 1997, **166**, 223–230.
40. E. L. P. Y. Biancá, J. Desimoni and N. E. Christensen: *Phys. B*, 2004, **354B**, 341–344.
41. L. J. E. Hofer and E. M. Cohn: *J. Am. Chem. Soc.*, 1958, **81**, 1576–1582.
42. K. Reuter and M. Scheffler: *Phys. Rev. B*, 2001, **65B**, 035406–035416.
43. K. Reuter and M. Scheffler: *Phys. Rev. B*, 2003, **68B**, 045407–045417.
44. B. Hammer, L. B. Hansen and J. K. Nørskov: *Phys. Rev. B*, 1999, **59B**, 7413–7421.
45. W. Tang, E. Sanville and G. Henkelman: *J. Phys.: Condens. Matter*, 2009, **21**, 084204–084210.
46. E. Sanville, S. D. Kenny, R. Smith and G. Henkelman: *J. Compos. Chem.*, 2007, **28**, 899–908.
47. G. Henkelman, A. Arnaldsson and H. Jónsson: *Comput. Mater. Sci.*, 2006, **36**, 254–360.
48. O. Karabelchtchikova: 'Fundamentals of mass transfer in gas carburizing', PhD thesis, Worcester Polytechnic Institute, Worcester, MA, USA, 2008.
49. H. M. T. Galvis, J. H. Bitter, T. Davidian, M. Ruitenbeek, A. L. Dugulan and K. P. de Jong: *J. Am. Chem. Soc.*, 2012, **134**, 16207–16215.
50. M. D. Shroff, D. S. Kalakkad, K. E. Coulter, S. D. Kohler, M. S. Harrington, N. B. Jackson, A. G. Sault and A. K. Datye: *J. Catal.*, 1995, **156**, 185–207.
51. R. J. O'Brien, L. Xu, R. L. Spicer and B. H. Davis: *Eng. Fuels*, 1996, **10**, 921–926.
52. P. Sautet and F. Cinquini: *Chem. Cat. Chem.*, 2010, **2**, 636–639.
53. R. G. Olsson and E. T. Turkdogan: *Metall. Trans.*, 1974, **5**, 21–26.
54. R. Asano, Y. Sasaki and K. Ishii: *ISIJ Int.*, 2002, **42**, 121–126.
55. J. Q. Zhang, A. Schneider and G. Inden: *Corros. Sci.*, 2003, **45**, 281–299.
56. M. Watanabe and P. Wissmann: *Catal. Lett.*, 1991, **1**, 15–26.
57. C. M. Chun, T. A. Ramamarayanan and J. D. Mumford: *Mater. Corros.*, 1999, **50**, 634–639.
58. J. B. Butt: *Catal. Lett.*, 1990, **7**, 83–106.
59. H. J. Grabke: *Mater. Corros.*, 1998, **49**, 303–308.
60. A. C. J. Koeken, H. M. T. Galvis, T. Davidian, M. Ruitenbeek and K. P. de Jong: *Angew. Chem. Int. Ed.*, 2012, **51**, 7190–7193.
61. S. Ando and H. Kimura: *Scr. Metall.*, 1989, **23**, 1767–1772.
62. L. P. Zhou: 'Kinetic study of the Fischer-Tropsch synthesis over an industrial iron-based catalyst', PhD thesis, Institute of Coal Chemistry, Chinese Academy of Sciences, China, 2011.
63. E. de Smit, M. M. van Schooneveld, F. Cinquini, H. Bluhm, P. Sautet, F. M. F. de Groot and B. M. Weckhuysen: *Angew. Chem. Int. Ed.*, 2011, **50**, 1584–1588.
64. E. J. Fasiska and G. A. Jeffrey: *Acta Crystallogr.*, 1965, **19**, 463–471.
65. D. Fruchart, P. Chaudouet, R. Fruchart, A. Rouault and J. P. Senateur: *J. Solid. State. Chem.*, 1984, **51**, 246–252.
66. K. Momma and F. Izumi: *J. Appl. Crystallogr.*, 2011, **44**, 1272–1276.
67. S. V. Khare, S. Kodambaka, D. D. Johnson, I. Petrov and J. E. Greene: *Surf. Sci.*, 2003, **522**, 75–83.
68. N. D. Spencer, R. C. Schoonmaker and G. A. Somorjai: *J. Catal.* 1982, **74**, 129–135.
69. V. R. Stamenkovic, B. Fowler, B. S. Mun, G. F. Wang, P. N. Ross, C. A. Lucas and N. M. Markovic: *Science*, 2007, **315**, 493–497.
70. J. Dubois, T. Epicier, C. Esnouf, G. Fantozzi and P. Convert: *Acta Metall.*, 1988, **36**, 1891–1901.
71. D. H. Jack and K. H. Jack: *Mater. Sci. Eng.*, 1973, **11**, 1–27.
72. K. H. Jack: *Acta Cryst.* 1950, **3**, 392–394.
73. R. G. Crespo, S. Hamad, C. R. A. Catlow and N. H. de Leeuw: *J. Phys.: Condens. Matter*, 2007, **19**, 256201–256216.
74. L. J. E. Hofer, E. M. Cohn and W. C. Peebles: *J. Am. Chem. Soc.*, 1949, **71**, 189–195.
75. D. C. Gardner and C. H. Bartholomew: *Ind. Eng. Chem. Prod. Res. Dev.*, 1981, **20**, 80–87.
76. P. L. Walker Jr, J. F. Rakszawski and G. R. Imperial: *J. Phys. Chem.*, 1959, **63**, 140–149.